Editors' Suggestion

Phase separation at the dimer-superconductor transition in Ir$_{1-x}$Rh$_x$Te$_2$

R. Yu,[1,*] S. Banerjee,[2] H. Lei,[1,†] M. Abeykoon,[3] C. Petrovic,[1] Z. Guguchia,[1,4] and E. S. Bozin[1,‡]

[1]*Condensed Matter Physics and Materials Science Department, Brookhaven National Laboratory, Upton, New York 11973, USA*
[2]*Department of Applied Physics and Applied Mathematics, Columbia University, New York, New York 10027, USA*
[3]*Photon Sciences Division, Brookhaven National Laboratory, Upton, New York 11973, USA*
[4]*Department of Physics, Columbia University, New York, New York 10027, USA*

The detailed evolution of the local atomic structure across the (x, T) phase diagram of transition metal dichalcogenide superconductor Ir$_{1-x}$Rh$_x$Te$_2$ ($0 \leqslant x \leqslant 0.3$, 10 K $\leqslant T \leqslant 300$ K) is obtained from high-quality x-ray diffraction data using the atomic pair distribution function (PDF) method. The observed hysteretic thermal structural phase transition from a trigonal ($P\bar{3}m1$) to a triclinic ($P\bar{1}$) dimer phase for low Rh content emphasizes the intimate connection between the lattice and electronic properties. For superconducting samples away from the dimer/superconductor phase boundary, structural transition is absent and the local structure remains trigonal down to 10 K. In the narrow range of compositions close to the boundary, PDF analysis reveals structural phase separation, suggestive of weak first-order character of the Rh-doping induced dimer-superconductor quantum phase transition. Samples from this narrow range show weak anomalies in electronic transport and magnetization, hallmarks of the dimer phase, as well as superconductivity albeit with incomplete diamagnetic screening. The results suggest that the dimer and superconducting orders exist in the mutually exclusive spatial regions.

I. INTRODUCTION

Appearance of superconductivity in the proximity and upon destabilization of other quantum states describes a number of complex electronic systems, as exemplified by the phase diagrams of unconventional superconductors [1,2]. Understanding how superconductivity emerges in these materials is among the central challenges in condensed matter physics. While long-range ordered phases are generally seen as detrimental for superconductivity, fluctuations of these phases are considered to have ties to superconducting pairing [3], but the details are intricate and still remain quite puzzling.

Layered transition metal dichalcogenides (TMD) as low dimensional solids provide an opportune platform to study various electronic instabilities, most notably the interplay between charge density wave (CDW) [4,5] and superconductivity (SC) [6,7]. Importantly, in some TMD classes, CDW can be readily tuned into SC by controlling system parameters such as the chemical composition and pressure [8–13] resulting in dome-shaped phase diagrams and linear dependence of T_c on the superfluid density [14], reminiscent of cuprates. The perceived similarity with cuprates that exhibit ubiquitous susceptibility to charge ordering [15–19] extends also to homologous pseudogaps [20–23]. Thus systematic explorations of TMDs are expected to provide further insights of relevance for the cuprate physics [17,24–26].

A polymorph of metallic iridium ditelluride, IrTe$_2$, displaying CdI$_2$-type structure [27], attracted considerable attention following the recent discovery of bulk superconductivity with $T_c \sim 3$ K in intercalated and/or Ir-site substituted derivates IrTe$_2$:Pd [28], Ir$_{1-x}$Pt$_x$Te$_2$ [29], Cu$_x$IrTe$_2$ [30], and Ir$_{1-x}$Rh$_x$Te$_2$ [31]. Given that superconductivity emerges upon suppression of a phase transition into an intriguing low-temperature CDW-like state associated with $\bm{q_0} = (1/5, 0, 1/5)$ instability [28,32], the discovery triggered a surge of research activity aimed at revealing the driving force behind this modulation and, ultimately, its relationship to superconductivity.

Below $T_s \sim 280$ K, IrTe$_2$ displays a first-order symmetry-lowering transition [33] from the high-temperature trigonal [$P\bar{3}m1$, Fig. 1(a)] [34] to a low-temperature triclinic [$P\bar{1}$, Fig. 1(b)] [35] phase. It is accompanied by sharp anomalies in electrical resistivity and magnetic susceptibility [33] akin to those seen in CDW bearing materials [36,37]. However, he mechanism turns out to be more complex than the Fermi surface nesting. This is evidenced by substantial electronic structure reconstruction [38], lack of discernible CDW gap features in spectroscopic measurements [38–41] and phonon softening instabilities in phonon dispersions [42], as well as observed pressure effects opposite to those expected for conventional CDW systems [43]. The low-temperature structure model obtained from single-crystal x-ray diffraction not only adequately accounts for the observed modulated state [28,32], but also reveals partial dimerization of Ir and Te sublattices and associated charge disproportionation [35,42,44] resulting in tremendous structural distortions [sketched in Fig. 1(c)]. Recent analysis based on first-principles total energy density functional theory calculations combined with angle-resolved photoemission spectroscopy indicates that, apart from a

*Present address: Institute of Physics, Chinese Academy of Science, Beijing 100190, People's Republic of China.
†Present address: Department of Physics, Renmin University, Beijing 100872, People's Republic of China.
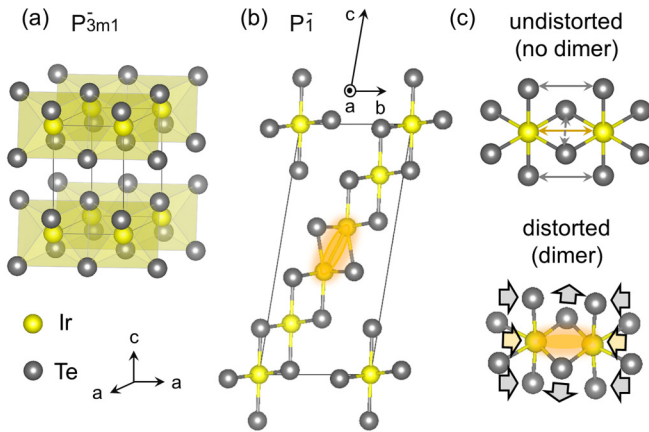‡bozin@bnl.gov

FIG. 1. Details of IrTe$_2$ structures. (a) Undistorted high-temperature trigonal model ($P\bar{3}m1$). (b) Distorted low-temperature triclinic model ($P\bar{1}$) featuring Ir dimers. (c) Sketch of local IrTe$_6$ octahedral environments expected in the absence/presence of Ir dimers (top/bottom). Dimerization results in dramatic distortions of associated interatomic distances relative to the high-temperature structure: Ir-Ir and Te-Te dimer distances reduce by 0.83 and 0.5 Å, respectively, while the lateral Te-Te distance elongates by 0.29 Å [35], as indicated by block arrows.

CDW-like instability, the uniform lattice deformation and the Ir dimerization play very important role [45].

It has been suggested that SC in chemically altered IrTe$_2$ variants competes with the low-T state in a quantum critical point (QCP) manner [28], and that fluctuations of this state possibly mediate superconductivity [29,46], tacitly implying similarity to unconventional SCs. Since most studies focus on the origin and mechanism of the phase transition [32,42,45–51], the question whether the suppression of the low-T phase with chemical doping proceeds in a first- or second-order (QCP-like) manner is still not resolved.

Strong coupling of the electronic state to the lattice enables utilization of local structure methods, such as the atomic pair distribution function (PDF) [52] and extended x-ray absorption fine structure (EXAFS) [53], to study the evolution of such a state across the doping-temperature, (x, T), phase diagrams of interest. Given the intimate involvement of the structure, the proposed fluctuations [28,29,46] should leave their footprint in the nanoscale atomic structure, which can be studied by the local probes sensitive to presence/absence of distortions irrespective of the length scale and character of their ordering. However, only a limited number of local structure studies of this system have been conducted to date. Two studies based on EXAFS are focused on undoped IrTe$_2$ under ambient [47] and high-pressure [54] conditions. The study of the transition under ambient conditions suggested that Ir dimers persist *locally* even in the high-temperature regime, despite the average structure being undistorted trigonal [47]. A recently reported PDF study of superconducting Ir$_{0.95}$Pt$_{0.05}$Te$_2$ and Ir$_{0.8}$Rh$_{0.2}$Te$_2$ did not find evidence of local fluctuating dimers in the superconducting regime, suggesting their absence [55]. This PDF study also did not find evidence of persisting dimer fluctuations in IrTe$_2$ at high temperature, in stark contrast to the EXAFS analysis based claims [47].

Here, we report results of detailed local structure characterization of Ir$_{1-x}$Rh$_x$Te$_2$ across the (x, T) phase diagram using an x-ray total scattering based PDF approach. The ability of the PDF method to reveal hidden nanometer scale structure aspects in a broad class of complex systems, including oxides and chalcogenides, which is important for more thorough understanding of their physical properties, is by now well established [56–62]. Ir$_{1-x}$Rh$_x$Te$_2$ displays an electronic phase diagram [31] very similar to that of other doped IrTe$_2$ variants, with superconductivity emerging close to $x = 0.1$, and involves substitution of Ir by isovalent Rh with nearly identical ionic radii, thereby providing the least involved stage to explore this matter. Our analysis directly maps out the suppression of *local* dimerization with Rh doping occurring in the same way on all length scales. The quantum phase transition from the long-range dimerized to the superconducting phase proceeds in a weakly first-order-like manner, as revealed by the observed intrinsic separation between nondimerized and dimerized phases in a narrow compositional range close to the dimer-superconductor phase boundary. In this range, the diamagnetic screening increases as the dimer fraction decreases, indicating that SC and dimers probably do not coexist within the same spatial regions. In addition, there is no evidence for local dimers persisting deep into the SC regime, in agreement with a previous report [55]. All these observations rule out the proposed QCP scenario.

II. EXPERIMENTAL

Polycrystalline samples of Ir$_{1-x}$Rh$_x$Te$_2$ $(0 \leqslant x \leqslant 0.3)$ were synthesized via the standard solid-state route. Stoichiometric amounts of elemental Ir, Rh, and Te were thoroughly mixed, ground, and pelletized. The pellets were placed in alumina crucibles, sealed into quartz tubes under 0.2 atm argon gas, and sintered at 1000° C for 15 h, followed by cooling to room temperature. The process was repeated with intermediate grindings to ensure chemical homogeneity. The samples were found to be in a single phase based on laboratory x-ray powder diffraction and displayed almost no variation of lattice parameters with Rh content, in agreement with a previous report [31]. The final stoichiometries were confirmed by explicit refinement of the site occupancies in the structural modeling of the room-temperature PDF data.

The experimental PDFs were obtained from the collected two-dimensional (2D) diffraction data using standard protocols [52,63] based on synchrotron x-ray total scattering measurements carried out at 28-ID-2 x-ray powder diffraction (XPD) beamline of National Synchrotron Light Source II at Brookhaven National Laboratory. The setup utilized a 67.7 keV x-ray beam ($\lambda = 0.183$ Å), and was equipped with a flat panel image plate detector based on amorphous silicon technology (Perkin Elmer). This setup is optimized such as to provide a broad Q-space coverage, and in turn enhanced r-space resolution, at the expense of Q-space resolution, as is standard in rapid data acquisition xPDF setups [64]. The temperature-dependent measurements in the 10–300 K range (5-K steps) were done on warming using a closed cycle helium cryostat (Cryoindustries of America) featuring an evacuated chamber with a holder accommodating simultaneously three samples, and a set of thin mylar windows. In order to explore
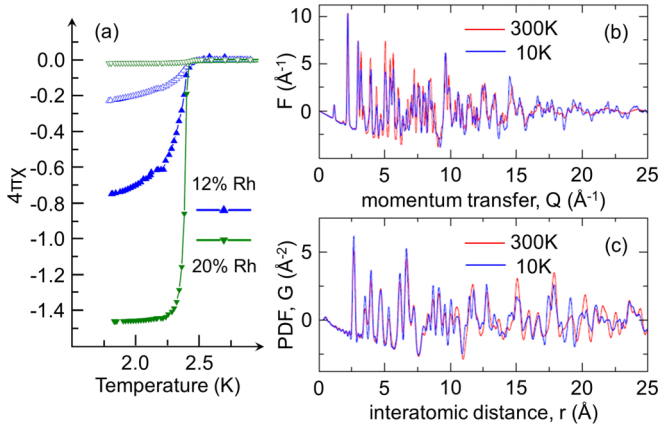
FIG. 2. Comparisons of magnetic susceptibility and total scattering data for selected $Ir_{1-x}Rh_xTe_2$ compositions: (a) dc susceptibility for $x = 0.12$ and 0.2 samples at H = 10 Oe in zero-field-cooling (solid symbols) and field-cooling (open symbols) modes at low-temperature. (b) Reduced total scattering functions, $F(Q)$, and (c) xPDFs, $G(r)$, for $x = 0$ sample at 300 (red) and 10 K (blue).
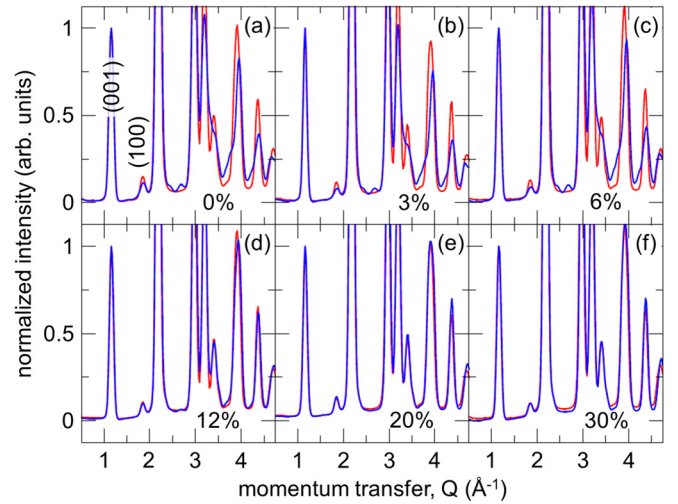

FIG. 3. Comparison of azimuthally integrated 2D diffraction patterns of $Ir_{1-x}Rh_xTe_2$ for 300 (solid red line) and 10 K (solid blue line) over a narrow range of momentum transfer Q for (a) $x = 0$, (b) 0.03, (c) 0.06, (d) 0.12, (e) 0.2, and (f) 0.3. All patterns are normalized by the intensity of (001) reflection ($P\overline{3}m1$ indexing).

the system behavior on thermal cycling, additional measurements over the 80–300 K range were performed for all the samples on cooling and successive warming using a liquid nitrogen based cryostream (Oxford Cryosystems 700). The raw 2D diffraction data were integrated and converted to intensity versus Q using the software FIT2D [65], where Q is the magnitude of the scattering vector. Data reduction to measured total scattering structure functions, $F(Q)$ [Fig. 2(b)], and their successive sine Fourier transform up to a momentum transfer of $Q_{max} = 25$ Å^{-1} to obtain experimental PDFs, $G(r)$ [Fig. 2(c)], were carried out using the PDFGETX3 [63] program. PDF structure refinements using models based on $P\overline{3}m1$ and $P\overline{1}$ symmetries were carried out using the PDFGUI program suite [66].

III. RESULTS AND DISCUSSION

We begin by qualitatively comparing the data of parent $IrTe_2$ at endpoint temperatures (300 and 10 K) to assess the sensitivity of the total scattering approach to the symmetry lowering occurring across its structural phase transition [33,35,39,42]. Despite the rather poor Q-space resolution, the effects of symmetry lowering are apparent in the integrated data presented in the form of a derived reduced total scattering function, $F(Q)$ [Fig. 2(b)]. The peaks in, for example, 5–10 Å^{-1} range appear visibly sharper for 300 K (solid red line) than for 10 K (solid blue line), despite the opposite being expected due to the Debye-Waller effects at high-temperature. In the corresponding PDFs, one readily observes the appearance of new peaks in the 10-K $G(r)$ profile as compared to its 300 K counterpart, particularly apparent at, e.g., interatomic distances larger than 10 Å in Fig. 2(c). This establishes the sensitivity of both Q-space and r-space variants of our data to the symmetry lowering observed in $IrTe_2$.

A similar qualitative survey can then be extended to all the samples in the $Ir_{1-x}Rh_xTe_2$ series. Figure 3 provides a

comparison of diffraction patterns obtained by azimuthal integration of the raw 2D data. The patterns are further normalized by the intensity of (001) reflection ($P\overline{3}m1$ notation). Profiles in red correspond to 300 K, while profiles in blue represent 10 K. Samples with 0%, 3%, and 6% Rh display very similar behavior with the global symmetry lowered in the 10-K data as evident from additional, although poorly resolved, peaks emerging in the low-temperature patterns shown in Figs. 3(a)–3(c). The data for 300 K are also sharper than the data at 10 K, consistent with the lower symmetry at base temperature. On the other hand, no additional peaks appear at low-temperature for 20% and 30% Rh compositions, with 10 K profiles visibly sharper than those corresponding to 300 K [Figs. 3(e) and 3(f)], as expected from Debye-Waller effects in a system where global symmetry does not change [67], and opposite to what is observed for lower Rh concentrations. Given the limited Q-space resolution of our measurement, this observation does not immediately rule out the average symmetry lowering in these samples, but such conclusion would certainly be in line with the lack of observable anomalies in electrical resistivity and magnetic susceptibility for these Rh concentrations [31]. Samples with intermediate compositions close to the dimer/superconductor boundary [31] show an appreciably weaker response than those with low Rh-content, but still consistent with there being a structural change. This is shown for 12% composition in Fig. 3(d), with similar behavior also observed for the 10% Rh sample (not shown). This assessment indicates that the average structure changes up to and possibly including compositions close to the dimer/superconductor boundary, while it remains unchanged in the superconducting region of compositions.

Qualitative comparisons of as measured (without any scaling) PDFs, shown in Fig. 4 over the range of 10 Å, provide further noteworthy insights. At 300 K, all patterns are qualitatively very similar, with observable differences arising primarily in the PDF peak intensities, which is expected due to
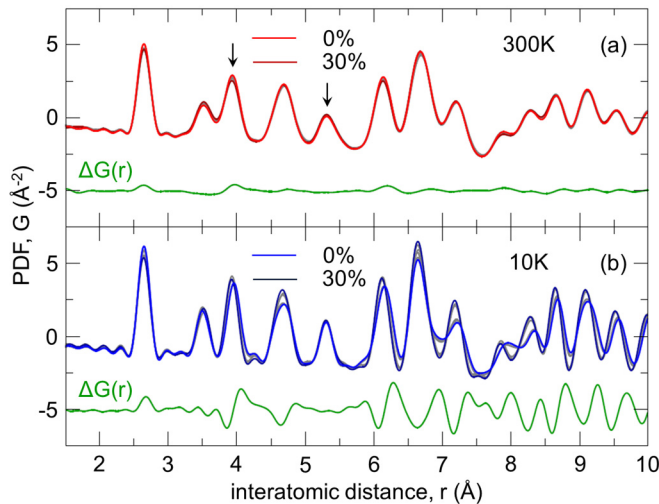
FIG. 4. Comparison of experimental xPDFs of $Ir_{1-x}Rh_xTe_2$ for $0 \leqslant x \leqslant 0.3$ over 10-Å range at (a) 300 and (b) 10 K. The data for the end members are shown as colored profiles, and for the intermediates as gray profiles. $\Delta G(r)$ in both panels represents the difference between $x = 0$ (light red/blue) and 0.3 (dark red/blue) xPDFs, shown as a solid green line and offset for clarity. At 300 K, all xPDF profiles look very similar. At 10 K, xPDF profiles apparently cluster into two groups, those resembling $x = 0$ (light blue), and those that are similar to $x = 0.3$ (dark blue). Arrows in (a) mark lattice repeat distance peaks in the trigonal phase.

the very different x-ray scattering form factors of Ir ($Z = 77$) and Rh ($Z = 45$) [52]. There is no observable variation with Rh content of the PDF peak positions, as can be seen by inspecting, e.g., the lattice repeat distance peaks centered around $a \approx 3.932$ Å and $c \approx 5.397$ Å marked by arrows in Fig. 4(a). This is consistent with the unchanged bond-length distribution and also consistent with the previously reported minute variability in lattice constants of $Ir_{1-x}Rh_xTe_2$ with Rh content at room temperature [31], in contrast to $Ir_{1-x}Pt_xTe_2$, where Pt doping alters the unit cell parameters appreciably [29]. This is exemplified by PDFs of 0% and 30% Rh data, shown in Fig. 4(a) as light red and dark red solid lines, respectively. Their difference, shown as green line underneath, displays signatures consistent with the PDF intensity variations. The profiles for all other compositions are superimposed as gray solid lines and gradually fill the small intensity gaps between the two PDFs corresponding to the end members and are virtually indistinguishable from already very similar end-member PDFs. Remarkably, the signal in the nonphysical region of r below 2.5 Å, and just before the nearest-neighbor peak, is exceptionally well matched across all data sets, with small ripples originating from the effects of the finite size of the Fourier transform window being well aligned for all Rh compositions. This reflects the exceptional reproducibility of PDF data across all seven studied samples with different Rh content, as well as the overall data quality [68].

On the other hand, the PDF data comparison at 10 K reveals quite different behavior. PDFs of 0% and 30% Rh data are shown in Fig. 4(b) as light blue and dark blue solid lines, respectively, with their difference (green line) reflecting additional positional mismatch characteristics of appreciable changes in the underlying bond-length distribution. This is
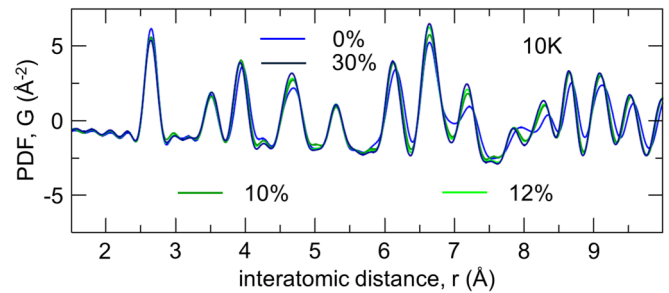

FIG. 5. Comparison of experimental xPDFs of $Ir_{1-x}Rh_xTe_2$ over 10-Å range at 10 K for $x = 0$ (solid light blue line), 0.1 (solid dark green line), 0.12 (solid light green line), and 0.3 (solid dark blue line). See text for details.

consistent with a change in symmetry on going from one composition to another at base temperature. For the samples with in-between compositions, the PDFs are again displayed as gray profiles. These PDFs appear to cluster together with either the 0% Rh PDF or the 30% Rh PDF in almost perfect binary registry of two states, with no visible gradual change. However, careful inspection reveals that 10% and 12% compositions deviate somewhat from this trend and show an intermediate behavior on a length scale of approximately 1 nm (Fig. 5), suggestive of possible phase separation. Details of this behavior will be explored quantitatively and addressed further below.

Next, we characterize the local structure evolution more quantitatively by explicitly fitting the structure models to the experimental PDF data using a full profile least squares approach, similar to that of the Rietveld method [69] in conventional powder diffraction as described in detail elsewhere [66]. Data at 300 K for all the samples are found to conform to trigonal $P\bar{3}m1$ model of $IrTe_2$ [33], and all obtained fits are of comparably good quality as shown in Fig. 6, consistent with all the samples being single phase. In order to map out the structural evolution with temperature and doping, and to observe the areas of the phase diagram where the local symmetry is broken, we utilize a high-temperature trigonal $P\bar{3}m1$ model for all the data of all the samples first. In this approach, a high-symmetry model is used to detect the locally broken symmetry by charting locations in an (x, T) phase diagram where such model fails to explain the PDF data. This is typically done by monitoring the evolution of the weighted fit residual, r_W, which quantifies the goodness of the fit of the used model [66]. Additionally, atomic displacement parameters (ADP), U, are also monitored, as these become anomalously enhanced when the underlying symmetry is lowered thus indicating inadequacy of the model to explain the established distortions [70,71]. This simple yet powerful approach has been very successful in detecting presence of low-temperature nanoscale Ir-dimer fluctuations in $Cu(Ir_{1-x}Cr_x)_2S_4$ thiospinel [62] for Cr concentrations for which long-range dimer order is not observed [72], as mentioned earlier, an information crucial for comprehensive understanding of observed anomalies in electronic transport in that system [62].

The results of this approach applied to $Ir_{1-x}Rh_xTe_2$ by utilizing the $P\bar{3}m1$ model over 50 Å range are summarized
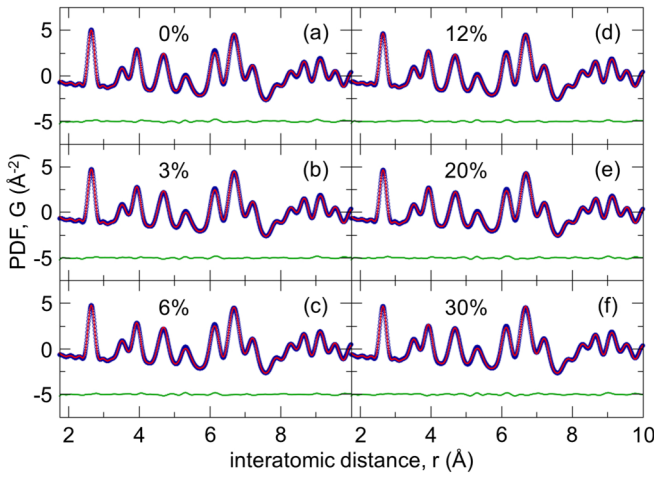
FIG. 6. Structural refinements of $P\bar{3}m1$ model (solid red line) to $Ir_{1-x}Rh_xTe_2$ xPDF data at 300 K (open blue symbols) over 10-Å range. The difference between the data and the model is shown as a solid green line underneath and is offset for clarity. (a) $x = 0$ ($r_W = 3.9\%$), (b) $x = 0.03$ ($r_W = 3.8\%$), (c) $x = 0.06$ ($r_W = 4.1\%$), (d) $x = 0.12$ ($r_W = 4.2\%$), (e) $x = 0.2$ ($r_W = 4.1\%$), and (f) $x = 0.3$ ($r_W = 4.1\%$). Refinement of $x = 0.1$ data (not shown) results in a fit with residual of $r_W = 3.9\%$.

in Fig. 7. Both fit residual, Fig. 7(a), and Ir ADP, Fig. 7(b), are found to exhibit abrupt upturns for $IrTe_2$ at temperatures where anomalies in resistivity and susceptibility set in, evidencing (this time directly) the onset of structural transformation. Very similar anomalies are also seen in doped samples with Rh content up to and including 12%, with the transition temperature gradually decreasing and the transition generally becoming broader with increasing Rh content, in line with the temperature evolution of magnetic and transport properties [31] confirming coupling of the lattice degrees of freedom and the underlying physical properties [39]. For superconducting 20% and 30% Rh compositions away from the dimer/superconuctor phase boundary, anomalous upturns in the residual and Ir ADP fits are *not* observed down to the lowest accessible temperature (10 K), confirming that the average transition does not occur in these samples, and, more importantly, indicating absence of dimer fluctuations within the sensitivity of our data and the analysis protocol [55]. The weak gradual temperature dependence of r_W noticeable for 20% and 30% compositions in Fig. 7(a) is not an indication of underlying locally broken symmetry. This is rather a consequence of fits generally performing better at higher temperature due to thermal broadening masking any imperfections in experimental data that only become apparent at lower temperature. If these were related to local symmetry breaking, they would also be seen in the temperature dependent Ir ADPs in Fig. 7(b), but these exhibit canonical behavior [55,62,67,70].

Inspection of the fits of the $P\bar{3}m1$ model to 10-K PDF data over 10-Å range further corroborates this conclusion. Model clearly fails for 0%, 3%, 6%, and 10% data, Figs. 8(a)–8(d), with slightly better fits for 10% composition. The model does visibly better for 12%, but the discrepancies observed in the difference curve, Fig. 8(e), appear to correlate with similar discrepancies seen for lower doping and the fit residual is still larger than that for 300 K. On the other hand, the $P\bar{3}m1$
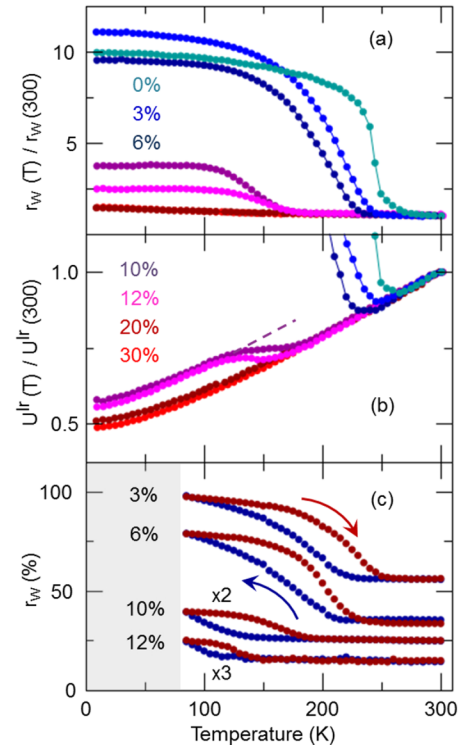

FIG. 7. Detection of structural transition in $Ir_{1-x}Rh_xTe_2$ by $P\bar{3}m1$ modeling of xPDF data. Rh content is indicated in the panels. (a) Fit residual, $r_W(T)$, normalized to 300 K value. (b) Isotropic atomic displacement parameter of Ir, $U(T)$, normalized to the 300-K value. (c) Fit residual, $r_W(T)$, for data collected on cooling (blue) and warming (red) for samples with selected Rh content. Hysteresis loops for 10% and 12% Rh samples are scaled for clarity, as indicated. Loops have been offset for clarity. Quantities shown in (a) and (b) are based on data acquired on warming using cryostat equipment; these shown in (c) are based on data collected on thermal cycling utilizing cryostream equipment. The shaded area in (c) denotes lack of data in the collection mode used.

model fits to 20% [Fig. 8(f)] and 30% data at 10 K are of comparable quality to those observed for the same model and samples at 300 K, indicating that this model provides a good description of the local structure for these compositions at low temperature and thus confirming that no observable dimer fluctuations are present [55].

In order to determine the character of the transition in Rh-substituted samples, the same approach is applied to the data obtained during thermal cycling. The transition is found to display observable hysteresis in the parameters sensitive to the transition for all the samples where it occurs, as shown in Fig. 7(c), indicating first-order behavior. Notably, the response becomes substantially weaker as Rh composition approaches the dimer/superconductor boundary, with the characteristic upturns in both the fit residual and Ir ADP measures nearly an order of magnitude smaller than for $IrTe_2$. This is consistent with there being a considerable reduction in the dimer density as the dimer/superconductor boundary is approached [55].

At this point, and before proceeding to low-temperature structure assessment, it is important to note that orderings other than 1/5 with higher dimer densities have also been observed in the $IrTe_2$ system. A second phase transition has
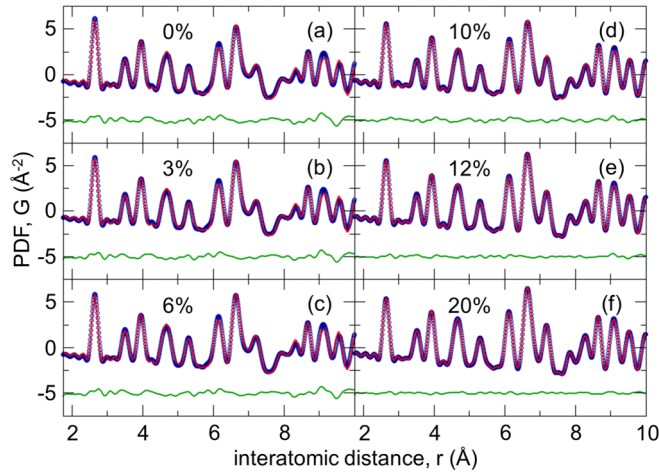
FIG. 8. Structural refinements of $P\bar{3}m1$ model (solid red line) to $Ir_{1-x}Rh_xTe_2$ xPDF data at 10 K (open blue symbols) over 10-Å range. Difference between the data and the model is shown as solid green line underneath (offset for clarity). (a) $x = 0$ ($r_W = 14.8\%$), (b) $x = 0.03$ ($r_W = 13.5\%$), (c) $x = 0.06$ ($r_W = 12.9\%$), (d) $x = 0.1$ ($r_W = 7.7\%$), (e) $x = 0.12$ ($r_W = 5.7\%$), and (f) $x = 0.2$ ($r_W = 3.9\%$). Refinement to $x = 0.3$ data (not shown) gives a similar quality fit to that for $x = 0.2$.
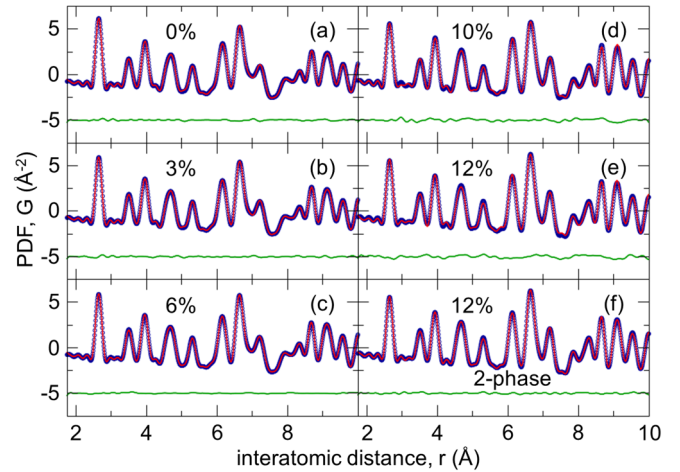

FIG. 9. Structural refinements at 10 K. Fits of $P\bar{1}$ model to the data of (a) $x = 0$ ($r_W = 2.0\%$), (b) $x = 0.03$ ($r_W = 2.1\%$), (c) $x = 0.06$ ($r_W = 2.3\%$), (d) $x = 0.1$ ($r_W = 6.3\%$) and (e) $x = 0.12$ ($r_W = 7.3\%$). (f) $P\bar{3}m1 + P\bar{1}$ two-phase model refinement to $x = 0.12$ data ($r_W = 2.7\%$). See text for details.

been reported to occur around $\sim$180 K from 1/5 to a higher dimer density 1/6 ordering state (presumed to be the ground state) [73], originally observed to occur as a function of Se doping in $IrTe_{2-x}Se_x$ [32], and confirmed in several followup studies [46,48–50,74,75]. However, one of the consequent studies revealed that the appearance of additional phases (beyond the 1/5 phase) is by no means ubiquitous, and that it very much depends on the sample synthesis protocols used [76]. The temperature-dependent assessments of our samples shown above do not exhibit any additional anomalies at lower temperature that could be attributed to presence of such higher dimer density phases in our samples. We therefore consider the local structure evolution at low-temperature within the framework of 1/5 ordering model.

For assessment of the local structure at low-temperature, the $P\bar{1}$ dimer model [Fig. 1(b)] with eight atoms in the asymmetric unit cell (three Ir and five Te atoms) is used to fit the PDF data at 10 K over a 10-Å range, utilizing lattice and fractional coordinate parameters as reported in the original single-crystal x-ray diffraction work of Pascut *et al.* [35]. Although this dimer model has considerably simpler unit cell than one previously reported in P1 setting by Cao *et al.* [42] (75 independent atoms: 25 Ir and 50 Te), it still has six lattice parameters and 21 independent fractional coordinates, a large number of variables as compared to three (two lattice parameters and one fractional coordinate) needed to describe the $P\bar{3}m1$ high-temperature structure. In order to avoid over-parametrization of the fits due to narrow PDF refinement range, we kept these parameters fixed to values reported for $IrTe_2$ [35], and refined only the overall scale factor and ADPs. The later were additionally constrained to be the same for the atoms of the same type. Even with this rather conservative approach, fits with exceptionally good agreement are achieved to the data for 0%, 3%, and 6% Rh compositions, as evident from Figs. 9(a)–9(c). Interestingly, this approach gave fits an

observably poorer quality for 10% and 12% Rh data, with the fit of the later being slightly worse than the fit of the former, as indicated by the values of the fit residual and also observable in the corresponding difference curves in Figs. 9(d) and 9(e). We recall here the qualitative comparison of 10-K PDF data (Fig. 5). There, one readily observes that data for 10% and 12% Rh samples display an intermediate behavior between that of low and high Rh content compositions, suggestive of a two-phase behavior. The increasing inability of the triclinic model to explain these data alone also points to a necessity to explore a two-phase mixture. Following this, these data were fit using an explicit two-phase modeling approach. The ingredient phases of this refinement were $P\bar{1}$ and $P\bar{3}m1$ using parameters for $IrTe_2$ at 10 and 300 K, respectively. These parameters were kept fixed, while refining one ADP for Ir and one for Te (shared across the phases), and one unique phase scale factor. This resulted in fits with significantly improved agreement as compared to cases when the two phases were refined independently within single phase refinements, as illustrated in Fig. 9(f) for 12% Rh data. The resulting phase fractions are 0.6(1) and 0.3(1) for 10% and 12% Rh samples at 10 K, respectively. We also estimated the dimer phase fraction from magnetic susceptibility measurements [77] and reported the Rh-content dependent size of the dip at the transition [31], normalized to its $x = 0$ value [55]. This shows good general agreement with the phase fraction estimated from the PDF analysis. Admittedly, in the PDF modeling of 10-K data of the undoped and low Rh-doped samples, the $P\bar{1}$ model results in fits of comparable quality to those of the two-phase model. This implies that the variation of the dimer density in this part of the phase diagram is relatively small and below the sensitivity of our approach [55], making the fraction of $P\bar{3}m1$ phase effectively inaccessible.

We summarize all observations resulting from the PDF analysis in a phase diagram shown in Fig. 10. The structure transition temperatures were determined as midpoint values obtained from the temperature dependence of parameters indicating failures of the $P\bar{3}m1$ model shown in Fig. 7. These
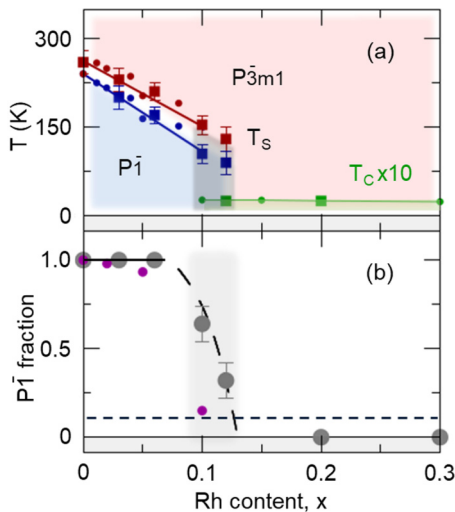
FIG. 10. (a) (x, T) phase diagram of $Ir_{1-x}Rh_xTe_2$. Solid blue and red circles represent magnetic phase transition temperature obtained from susceptibility measurements on cooling and warming, while the solid green circles denote superconducting transition temperature, after reference [31]. Solid blue and red squares mark the structural transition temperature in $Ir_{1-x}Rh_xTe_2$ from this study. Solid green squares denote superconducting transitions observed in samples used here. The values of superconducting T_c are multiplied by a factor of 10 for clarity. (b) $P\bar{1}$ phase fraction obtained from local structure refinements (solid gray symbols). The same phase fraction deduced from susceptibility measurements reported by Kudo *et al.* [31] (solid magenta circles). All lines are guides to the eye. Horizontal dashed line in (b) marks the estimated PDF sensitivity threshold to the presence of the local dimer phase [55].

are in generally good agreement with those reported from the measurements of the physical properties in $Ir_{1-x}Rh_xTe_2$ [31]. The superconducting temperatures for our samples were determined from dc susceptibility measurements. These are shown for two of our samples in Fig. 2(a). Although demagnetization corrections have not been done, these measurements suggest that the 12% Rh sample does not exhibit complete diamagnetic screening, whereas the 20% sample does. In addition, the 12% sample shows broader SC transition with weak pinning signatures as compared to the 20% sample. This clearly indicates that there is an enhancement of superconductivity with doping. On the other hand, the dimerized phase fraction [Fig. 10(b)] sharply decreases upon approaching the dimer/superconductor boundary on increasing Rh content, having the opposite trend to the superconducting fraction. This indicates that SC and dimerized phases likely do not coexist within the same spatial regions of the sample and that they are mutually exclusive.

The competitive nature of the interplay between SC and 1/5-dimer phase is also manifested in the following observations. Bulk superconductivity occurs without the presence of this phase in structural polymorphs of $IrTe_2$ other than trigonal, which have $IrTe_6$ connectivity different than edge sharing [78–81]. Apart from the character of the structural phase, significant depletion of the carrier density [82] accompanying the 1/5-ordering has been recently suggested as one of the contributing factors to the suppression of superconduc-

tivity. Recent STM studies also pointed to the incompatibility of the dimer phase and superconductivity, evidenced as nanoscale phase separation between these phases [82]. The adverse effect of dimerization is further seen in $AuTe_2$ [83] and $CuIr_2S_4$ [77] chalcogenides, where SC emerges as well only upon doping induced breaking of Te and Ir dimers, respectively. However, in $IrTe_2$, SC appears to be compatible with honeycomb-type charge order [82], suggesting that SC may couple only to a specific type of ordering [82,84].

IV. CONCLUSIONS

In summary, the nanometer scale structure of $Ir_{1-x}Rh_xTe_2$ has been studied across the (x, T) phase diagram by means of high-energy x-ray total scattering based atomic PDF analysis. The PDF data at 300 K for all samples $(0 \leqslant x \leqslant 0.3)$ studied are equally well explained by the trigonal $P\bar{3}m1$ model, indicating their single-phase character within the sensitivity of our data. PDF analysis evidences a structural phase transition for all compositions up to $x = 0.12$, and no structural change for $x = 0.2$ and 0.3 down to the lowest accessible temperature (10 K). The structural phase transition temperature gradually decreases with increasing Rh content, and shows a thermal hysteresis consistent with previous transport and susceptibility measurements. For samples with compositions away from the dimer/superconductor phase boundary, the base temperature PDF data are well explained by single-phase models. However, samples with compositions close to to the boundary $(x = 0.1$ and 0.12) are found to display separation into nondimerized $(P\bar{3}m1)$ and dimerized $(P\bar{1})$ phases as evidenced by explicit two-phase refinements of the PDF data. Qualitative measures of the transition become nearly order of magnitude weaker for the compositions close to the boundary, implying that the dimer density drops considerably as the superconducting regime is approached. Given the apparent reciprocal relationship between the doping evolution of the diamagnetic screening and the dimer fraction, the study suggests that below T_c, superconductivity emerges in the nondimerized region of the sample. This points to the macroscopic phase separation between dimer and superconducting phases, further reinforcing the idea of their competitiveness. Our results do not support the view of quantum critical behavior and further implicate that dimer fluctuations do not play significant role in the observed superconducting properties. The analysis carried out here does not rule out a possibility of ordering other than 1/5(1,0,1) in the regions of the phase diagram where dimerization is observed. However, absence of any additional anomalies in $P\bar{3}m1$ ADPs and fit residuals other than those associated with 1/5-order indicates that the cascade of phase transitions to states with different ordering vectors is not present in our samples.

[1] D. N. Basov and A. V. Chubukov, Nat. Phys. **7**, 272 (2011).

[2] L. Jiao, Y. Chen, Y. Kohama, D. Graf, E. Bauer, J. Singleton, J. Zhu, Z. Weng, G. Pang, T. Shang *et al.*, Proc. Natl. Acad. Sci. USA **112**, 673 (2015).

[3] J. C. Davis and D. Lee, Proc. Natl. Acad. Sci. USA **110**, 17623 (2013).

[4] K. Rossnagel, J. Phys.: Condens. Matter **23**, 213001 (2011).

[5] P. Monceau, Adv. Phys. **61**, 325 (2012).

[6] T. Valla, A. V. Fedorov, P. D. Johnson, J. Xue, K. E. Smith, and F. J. DiSalvo, Phys. Rev. Lett. **85**, 4759 (2000).

[7] A. H. Castro Neto, Phys. Rev. Lett. **86**, 4382 (2001).

[8] E. Morosan, H. W. Zandbergen, B. S. Dennis, J. W. G. Bos, Y. Onose, T. Klimczuk, A. P. Ramirez, N. P. Ong, and R. J. Cava, Nat. Phys. **2**, 544 (2006).

[9] B. Sipos, A. F. Kusmartseva, A. Akrap, H. Berger, L. Forro, and E. Tutis, Nat. Mater. **7**, 960 (2008).

[10] Y. Liu, R. Ang, W. J. Lu, W. H. Song, L. J. Li, and Y. P. Sun, Appl. Phys. Lett. **102**, 192602 (2013).

[11] P. Xu, J. O. Piatek, P.-H. Lin, B. Sipos, H. Berger, L. Forró, H. M. Rønnow, and M. Grioni, Phys. Rev. B **81**, 172503 (2010).

[12] R. Ang, Y. Miyata, E. Ieki, K. Nakayama, T. Sato, Y. Liu, W. J. Lu, Y. P. Sun, and T. Takahashi, Phys. Rev. B **88**, 115145 (2013).

[13] M. M. Ugeda, A. J. Bradley, Y. Zhang, S. Onishi, Y. Chen, W. Ruan, C. Ojeda-Aristizabal, H. Ryu, M. T. Edmonds, H. Tsai *et al.*, Nat. Phys. **12**, 92 (2016).

[14] Z. Guguchia, F. von Rohr, Z. Shermadini, A. T. Lee, S. Banerjee, A. R. Wieteska, C. A. Marianetti, B. A. Frandsen, H. Luetkens, Z. Gong *et al.*, Nat. Commun. **8**, 1082 (2017).

[15] J. M. Tranquada, B. J. Sternlieb, J. D. Axe, Y. Nakamura, and S. Uchida, Nature (London) **375**, 561 (1995).

[16] M. Hücker, M. v. Zimmermann, G. D. Gu, Z. J. Xu, J. S. Wen, G. Xu, H. J. Kang, A. Zheludev, and J. M. Tranquada, Phys. Rev. B **83**, 104506 (2011).

[17] E. H. da Silva Neto, P. Aynajian, A. Frano, R. Comin, E. Schierle, E. Weschke, A. Gyenis, J. Wen, J. Schneeloch, Z. Xu *et al.*, Science **343**, 393 (2014).

[18] R. Comin, A. Frano, M. Yee, Y. Yoshida, H. Eisaki, E. Schierle, E. Weschke, R. Sutarto, F. He, A. Soumyanarayanan *et al.*, Science **343**, 390 (2014).

[19] R. Comin, R. Sutarto, F. He, E. H. da Silva Neto, L. Chauviere, A. Frano, R. Liang, W. N. Hardy, D. A. Bonn, Y. Yoshida *et al.*, Nat. Mater. **14**, 796 (2015).

[20] S. V. Borisenko, A. A. Kordyuk, A. N. Yaresko, V. B. Zabolotnyy, D. S. Inosov, R. Schuster, B. Büchner, R. Weber, R. Follath, L. Patthey *et al.*, Phys. Rev. Lett. **100**, 196402 (2008).

[21] D. V. Evtushinsky, A. A. Kordyuk, V. B. Zabolotnyy, D. S. Inosov, B. Büchner, H. Berger, L. Patthey, R. Follath, and S. V. Borisenko, Phys. Rev. Lett. **100**, 236402 (2008).

[22] S. V. Borisenko, A. A. Kordyuk, V. B. Zabolotnyy, D. S. Inosov, D. Evtushinsky, B. Büchner, A. N. Yaresko, A. Varykhalov, R. Follath, W. Eberhardt *et al.*, Phys. Rev. Lett. **102**, 166402 (2009).

[23] A. A. Kordyuk, S. V. Borisenko, V. B. Zabolotnyy, R. Schuster, D. S. Inosov, D. V. Evtushinsky, A. I. Plyushchay, R. Follath, A. Varykhalov, L. Patthey *et al.*, Phys. Rev. B **79**, 020504 (2009).

[24] M. R. Norman, D. Pines, and C. Kallin, Adv. Phys. **54**, 715 (2005).

[25] J. Chang, E. Blackburn, A. T. Holmes, N. B. Christensen, J. Larsen, J. Mesot, R. Liang, D. A. Bonn, W. N. Hardy, A. Watenphul *et al.*, Nat. Phys. **8**, 871 (2010).

[26] V. Thampy, M. P. M. Dean, N. B. Christensen, L. Steinke, Z. Islam, M. Oda, M. Ido, N. Momono, S. B. Wilkins, and J. P. Hill, Phys. Rev. B **90**, 100510 (2014).

[27] E. F. Hockings and J. G. White, J. Phys. Chem. **64**, 1042 (1960).

[28] J. J. Yang, Y. J. Choi, Y. S. Oh, A. Hogan, Y. Horibe, K. Kim, B. I. Min, and S.-W. Cheong, Phys. Rev. Lett. **108**, 116402 (2012).

[29] S. Pyon, K. Kudo, and M. Nohara, J. Phys. Soc. Jpn. **81**, 053701 (2012).

[30] M. Kamitani, M. S. Bahramy, R. Arita, S. Seki, T. Arima, Y. Tokura, and S. Ishiwata, Phys. Rev. B **87**, 180501 (2013).

[31] K. Kudo, M. Kobayashi, S. Pyon, and M. Nohara, J. Phys. Soc. Jpn. **82**, 085001 (2013).

[32] Y. S. Oh, J. J. Yang, Y. Horibe, and S.-W. Cheong, Phys. Rev. Lett. **110**, 127209 (2013).

[33] N. Matsumoto, K. Taniguchi, R. Endoh, H. Takano, and S. Nagata, J. Low Temp. Phys. **117**, 1129 (1999).

[34] S. Jobic, P. Deniard, R. Brec, J. Rouxel, A. Jouanneaux, and A. N. Fitch, Z. Anorg. Allg. Chem. **598**, 199 (1991).

[35] G. L. Pascut, K. Haule, M. J. Gutmann, S. A. Barnett, A. Bombardi, S. Artyukhin, T. Birol, D. Vanderbilt, J. J. Yang, S. Cheong *et al.*, Phys. Rev. Lett. **112**, 086402 (2014).

[36] J. A. Wilson, F. J. Di Salvo, and S. Mahajan, Adv. Phys. **24**, 117 (1975).

[37] R. H. Friend and A. D. Yoffe, Adv. Phys. **36**, 1 (1987).

[38] A. F. Fang, G. Xu, T. Dong, P. Zheng, and N. L. Wang, Sci. Rep. **3**, 1153 (2013).

[39] K. Mizuno, K. Magishi, Y. Shinonome, T. Saito, K. Koyama, N. Matsumoto, and S. Nagata, Physica B **312-313**, 818 (2002).

[40] D. Ootsuki, Y. Wakisaka, S. Pyon, K. Kudo, M. Nohara, M. Arita, H. Anzai, H. Namatame, M. Taniguchi, N. L. Saini *et al.*, Phys. Rev. B **86**, 014519 (2012).

[41] D. Ootsuki, S. Pyon, K. Kudo, M. Nohara, M. Horio, T. Yoshida, A. Fujimori, M. Arita, H. Anzai, H. Namatame *et al.*, J. Phys. Soc. Jpn. **82**, 093704 (2013).

[42] H. Cao, B. C. Chakoumakos, X. Chen, J. Yan, M. A. McGuire, H. Yang, R. Custelcean, H. D. Zhou, D. J. Singh, and D. Mandrus, Phys. Rev. B **88**, 115122 (2013).

[43] A. Kiswandhi, J. S. Brooks, H. B. Cao, J. Q. Yan, D. Mandrus, Z. Jiang, and H. D. Zhou, Phys. Rev. B **87**, 121107 (2013).

[44] T. Toriyama, M. Kobori, T. Konishi, Y. Ohta, K. Sugimoto, J. Kim, A. Fujiwara, S. Pyon, K. Kudo, and M. Nohara, J. Phys. Soc. Jpn. **83**, 033701 (2014).

[45] K. Kim, S. Kim, K.-T. Ko, J.-H. Lee, J. Park, J. J. Yang, S.-W. Cheong, and B. I. Min, Phys. Rev. Lett. **114**, 136401 (2015).

[46] J. Dai, K. Haule, J. J. Yang, Y. S. Oh, S.-W. Cheong, and W. Wu, Phys. Rev. B **90**, 235121 (2014).

[47] B. Joseph, M. Bendele, L. Simonelli, L. Maugeri, S. Pyon, K. Kudo, M. Nohara, T. Mizokawa, and N. L. Saini, Phys. Rev. B **88**, 224109 (2013).

[48] K. Kim, S. Kim, and B. I. Min, Phys. Rev. B **90**, 195136 (2014).

[49] G. L. Pascut, T. Birol, M. J. Gutmann, J. J. Yang, S.-W. Cheong, K. Haule, and V. Kiryukhin, Phys. Rev. B **90**, 195122 (2014).

[50] K. Takubo, R. Comin, D. Ootsuki, T. Mizokawa, H. Wadati, Y. Takahashi, G. Shibata, A. Fujimori, R. Sutarto, F. He *et al.*, Phys. Rev. B **90**, 081104 (2014).

[51] T. Mizokawa, J. Electron. Spec. Related Phenomena **208**, 78 (2016).

[52] T. Egami and S. J. L. Billinge, *Underneath the Bragg Peaks: Structural Analysis of Complex Materials*, 2nd ed. (Elsevier, Amsterdam, 2012).

[53] B. K. Teo, *EXAFS: Basic Principles and Data Analysis* (Springer-Verlag, New York, 1986).

[54] E. Paris, B. Joseph, A. Iadecola, C. Marini, H. Ishii, K. Kudo, S. Pascarelli, M. Nohara, T. Mizokawa, and N. L. Saini, Phys. Rev. B **93**, 134109 (2016).

[55] R. Yu, S. Banerjee, H. C. Lei, R. Sinclair, M. Abeykoon, H. D. Zhou, C. Petrovic, Z. Guguchia, and E. S. Bozin, Phys. Rev. B **97**, 174515 (2018).

[56] X. Qiu, T. Proffen, J. F. Mitchell, and S. J. L. Billinge, Phys. Rev. Lett. **94**, 177203 (2005).

[57] E. S. Božin, M. Schmidt, A. J. DeConinck, G. Paglia, J. F. Mitchell, T. Chatterji, P. G. Radaelli, T. Proffen, and S. J. L. Billinge, Phys. Rev. Lett. **98**, 137203 (2007).

[58] E. S. Božin, A. S. Masadeh, Y. S. Hor, J. F. Mitchell, and S. J. L. Billinge, Phys. Rev. Lett. **106**, 045501 (2011).

[59] A. M. Abeykoon, E. S. Božin, W.-G. Yin, G. Gu, J. P. Hill, J. M. Tranquada, and S. J. L. Billinge, Phys. Rev. Lett. **111**, 096404 (2013).

[60] K. R. Knox, A. M. M. Abeykoon, H. Zheng, W.-G. Yin, A. M. Tsvelik, J. F. Mitchell, S. J. L. Billinge, and E. S. Bozin, Phys. Rev. B **88**, 174114 (2013).

[61] S. A. J. Kimber, I. I. Mazin, J. Shen, H. O. Jeschke, S. V. Streltsov, D. N. Argyriou, R. Valenti, and D. I. Khomskii, Phys. Rev. B **89**, 081408 (2014).

[62] E. S. Božin, K. R. Knox, P. Juhás, Y. S. Hor, J. F. Mitchell, and S. J. L. Billinge, Sci. Rep. **4**, 4081 (2014).

[63] P. Juhás, T. Davis, C. L. Farrow, and S. J. L. Billinge, J. Appl. Crystallogr. **46**, 560 (2013).

[64] P. J. Chupas, X. Qiu, J. C. Hanson, P. L. Lee, C. P. Grey, and S. J. L. Billinge, J. Appl. Crystallogr. **36**, 1342 (2003).

[65] A. P. Hammersley, S. O. Svenson, M. Hanfland, and D. Hauserman, High Pressure Res. **14**, 235 (1996).

[66] C. L. Farrow, P. Juhás, J. Liu, D. Bryndin, E. S. Božin, J. Bloch, T. Proffen, and S. J. L. Billinge, J. Phys.: Condens. Matter. **19**, 335219 (2007).

[67] P. Debye, Ann. Phys.-Berlin **344**, 789 (1912).

[68] P. F. Peterson, E. S. Božin, T. Proffen, and S. J. L. Billinge, J. Appl. Crystallogr. **36**, 53 (2003).

[69] H. M. Rietveld, Acta Crystallogr. **22**, 151 (1967).

[70] E. S. Bozin, R. Zhong, K. R. Knox, G. Gu, J. P. Hill, J. M. Tranquada, and S. J. L. Billinge, Phys. Rev. B **91**, 054521 (2015).

[71] M. Shatnawi, E. S. Bozin, J. F. Mitchell, and S. J. L. Billinge, Phys. Rev. B **93**, 165138 (2016).

[72] R. Endoh, J. Awaka, and S. Nagata, Phys. Rev. B **68**, 115106 (2003).

[73] P.-J. Hsu, T. Mauerer, M. Vogt, J. J. Yang, Y. S. Oh, S.-W. Cheong, M. Bode, and W. Wu, Phys. Rev. Lett. **111**, 266401 (2013).

[74] Q. Li, W. Lin, J. Yan, X. Chen, A. G. Gianfrancesco, D. J. Singh, D. Mandrus, S. V. Kalinin, and M. Pan, Nat. Commun. **5**, 5358 (2014).

[75] A. Glamazda, K. Choi, P. Lemmens, J. J. Yang, and S. Cheong, New J. Phys. **16**, 093061 (2014).

[76] M. J. Eom, K. Kim, Y. J. Jo, J. J. Yang, E. S. Choi, B. I. Min, J.-H. Park, S.-W. Cheong, and J. S. Kim, Phys. Rev. Lett. **113**, 266406 (2014).

[77] G. Cao, T. Furubayashi, H. Suzuki, H. Kitazawa, T. Matsumoto, and Y. Uwatoko, Phys. Rev. B **64**, 214514 (2001).

[78] Y. Qi, S. Matsuishi, J. Guo, H. Mizoguchi, and H. Hosono, Phys. Rev. Lett. **109**, 217002 (2012).

[79] L. Li, T. F. Qi, L. S. Lin, X. X. Wu, X. T. Zhang, K. Butrouna, V. S. Cao, Y. H. Zhang, J. Hu, S. J. Yuan *et al.*, Phys. Rev. B **87**, 174510 (2013).

[80] J. Guo, Y. Qi, and H. Hosono, Phys. Rev. B **87**, 224504 (2013).

[81] X. Li, J.-Q. Yan, D. J. Singh, J. B. Goodenough, and J.-S. Zhou, Phys. Rev. B **92**, 155118 (2015).

[82] G. Cao, W. Xie, W. A. Phelan, J. F. DiTusa, and R. Jin, Phys. Rev. B **95**, 035148 (2017).

[83] K. Kudo, H. Ishii, M. Takasuga, K. Iba, S. Nakano, J. Kim, A. Fujiwara, and M. Nohara, J. Phys. Soc. Jpn. **82**, 063704 (2013).

[84] H. S. Kim, S. Kim, K. Kim, B. I. Min, Y. Cho, L. Wang, S. Cheong, and H. W. Yeom, Nano Lett. **16**, 4260 (2016).